Paper publicar[1] / ***Published paper*:**

Monjo, LL., Córcoles, F., and Pedra, J. (2015) Parameter estimation of squirrel-cage motors with parasitic torques in the torque–slip curve IET Electric Power Applications, 9. 377-387. Doi 10.1049/iet-epa.2014.0208

---

[1] Substituir per la citació bibliogràfica corresponent

Parameter estimation of squirrel-cage motors with parasitic torques in the torque-slip curve

Ll. Monjo, F. Córcoles and J. Pedra

Department of Electrical Engineering, ETSEIB-UPC, Av. Diagonal 647, Barcelona 08028, Spain.

E-mails: lluis.monjo@upc.edu, corcoles@ee.upc.edu, pedra@ee.upc.edu

Abstract: This paper studies parasitic torques in steady-state torque-slip curves of squirrel-cage induction motors. The curves of nine motors (small, medium and large size units), three of which were measured in the range $s = 2$ to $s = 0$, are analyzed. The torque-slip curves of eight of these nine motors differ significantly from the smooth curves predicted by the classical single- and double-cage models: a torque dip at large slips in the motoring regime and a noticeable torque increase in the braking regime occur. As parasitic torques have been traditionally associated with space harmonics, two single-cage chain models (which consider the space harmonics) are tested to fit the measured torque and current of the three measured motors: one neglects the skin effect, leading to the wrong torque prediction while the other (the classical chain model in the literature) considers the skin effect, leading to an accurate torque prediction.

1 Introduction

Since the squirrel-cage induction motor became the most common industrial load, manufacturers have accumulated large amounts of data on torque- and current-slip curves.

Generally, measured curves can be approximated by the classical single- and double-cage induction machine models. These classical models assume that stator and rotor windings are sinusoidally distributed. As a consequence, the air-gap mmf of a winding is a perfectly sinusoidal waveform, i.e., the air-gap mmf of a winding produced by current $i(t)$ can be expressed as a function of time and position angle x as

$$f(x,t) = F_1 \cdot \cos(x-\alpha) \cdot i(t) \qquad \left(F_1 = \frac{2}{\pi} N \xi_1\right), \tag{1}$$

where α is the winding magnetic axis of symmetry, and amplitude F_1 depends on the winding arrangement (number of turns N and winding factor for the fundamental wave, ξ_1, i.e., distribution, pitch, and skew factors). The classical models also assume an unslotted machine having uniform air-gap of length g. Thus, the air-gap

Table 1 Manufacturer data of squirrel-cage induction motors

Motor	P_N (kW)	U_N (V)	f_N (Hz)	PF_N	ω_N (r/min)	η_N (%)	T_{MAX}/T_N	T_{ST}/T_N	T_{MIN}/T_N	I_{ST}/I_N
#1	1.5	400	50	0.69	950	79.1	2.3	1.7	1.5	3.9
#2	4	400	50	0.80	1430	86.0	2.6	2.3	1.4	6.3
#3	4	400	50	0.75	1445	86.7	3.4	3.1	2.5	7.1
#4	15	400	50	0.81	985	91.0	2.8	2.1	1.5	6.6
#5	30	400	50	0.85	1475	92.0	2.2	2.4	1.7	5.0
#6	45	400	50	0.89	2960	94.1	2.8	3.0	2.2	7.1
#7	88	400	50	0.84	1479	94.7	3.4	3.2	2.0	7.6
#8	250	400	50	0.86	1490	97.0	2.4	1.4	1.1	8.0
#9	500	400	50	0.88	1488	95.8	2.4	2.1	1.8	6.5

flux density B is also sinusoidal:

$$B(x,t)=\mu_0\cdot g^{-1}\cdot f(x,t)=\mu_0\cdot g^{-1}\cdot F_1\cdot\cos(x-\alpha)\cdot i(t), \tag{2}$$

where μ_0 is the permeability of free space.

However, a considerable number of motors have torque irregularities (also called parasitic torques) near zero speed in the torque-slip curve [1][2]. Table 1 contains manufacturer data of the nine motors considered in this paper. The parasitic torques are illustrated in the small size motor curves of Fig. 1 (laboratory measurements of motors #1, #2 and #3 made by the authors) and in the medium size motor curves of Fig. 2 (manufacturer measurements of motors #4, #5 and #6). More evidence of torque irregularities can be found using software tools provided by some manufacturers [3][4]. These tools plot or provide data about torque- and current-slip curves of their motors, where torque irregularities can be easily detected for some motors. For instance, Fig. 3 shows the curves of motor #7 (obtained from [3]), where parasitic torques are evident. Another example can be found for

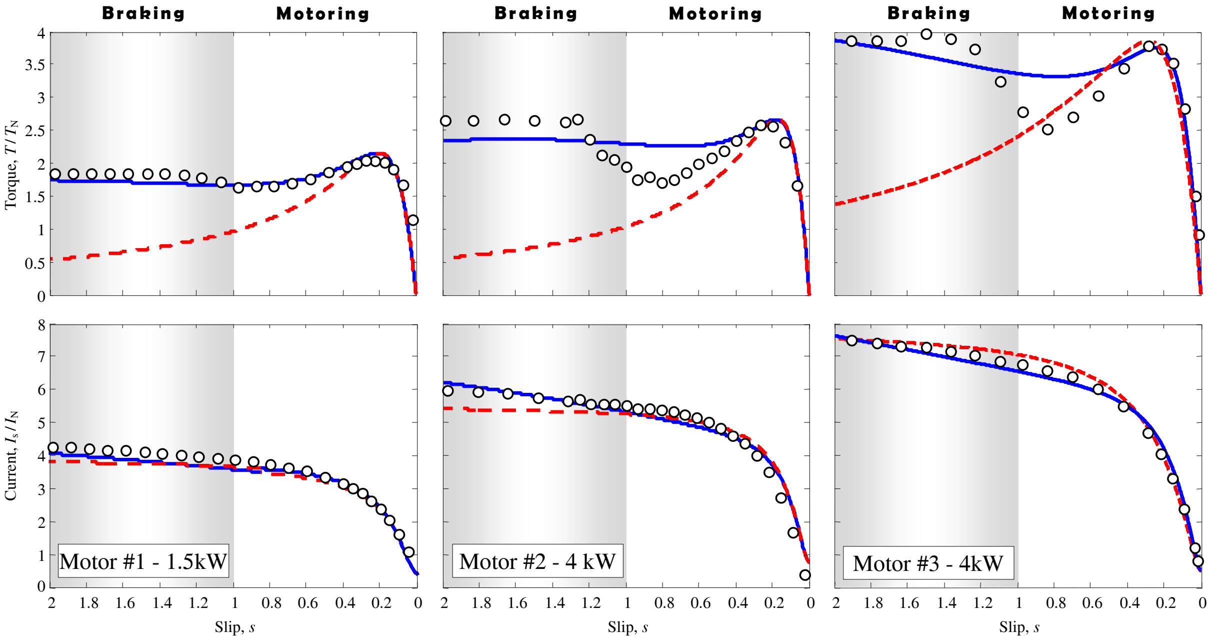

Fig. 1 *Measured torque- and current-slip data (circles) for the three tested small size motors. Curves estimated with the classical single- and double-cage models (broken and solid lines, respectively) are also drawn. Note that the measured range has been extended to the braking regime (shaded area).*

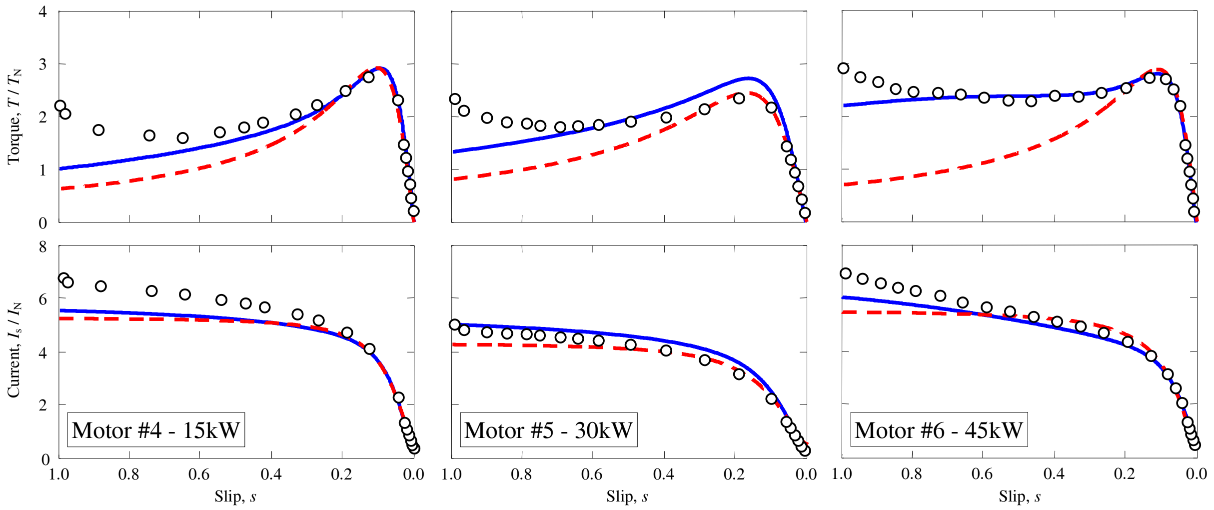

***Fig. 2** Measured torque- and current-slip data (circles) for the three tested medium size motors. Curves estimated with the classical single- and double-cage models (broken and solid lines, respectively) are also drawn.*

the large size motors #8 and #9 (obtained from [4]), where the minimum torque is lower than the starting torque ($T_{\mathrm{MIN}} / T_{\mathrm{ST}}$ is 0.78 and 0.86, respectively, Table 1). This is indicative of a torque-slip curve similar to that of the motors in Fig. 1, Fig. 2 and Fig. 3.

Fig. 1 and Fig. 2 also show that the classical double-cage model parameters (solid lines) estimated from the measurements clearly fail to predict the data measured for five of the six motors, and that the classical single-

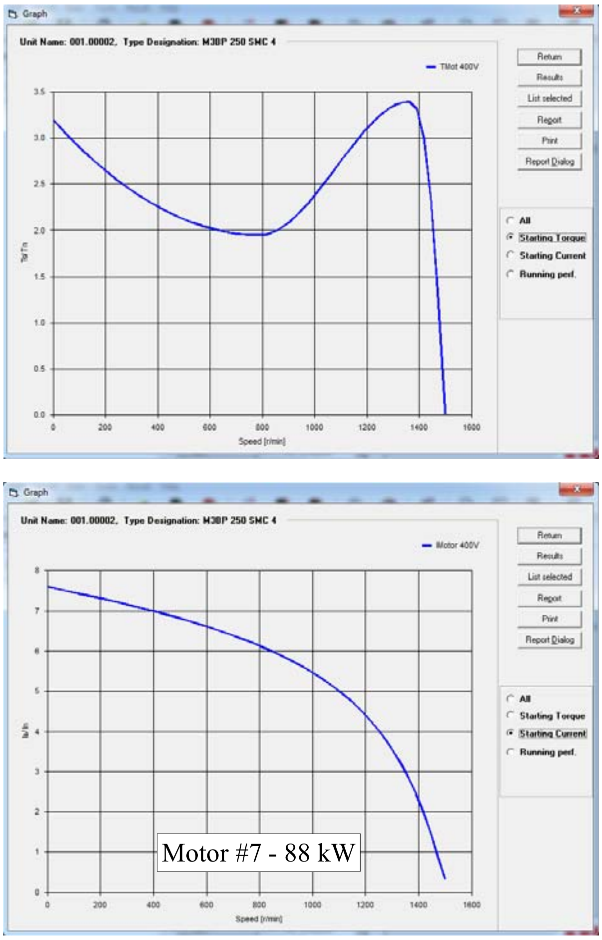
Unit Name: 001.00002, Type Designation: M3BP 250 SMC 4

○ All
● Starting Torque
○ Starting Current
○ Running perf.

Unit Name: 001.00002, Type Designation: M3BP 250 SMC 4

○ All
○ Starting Torque
● Starting Current
○ Running perf.

***Fig. 3** Torque- and current-slip curves provided by the manufacturer software for motor #7 [3].*

cage model parameters (broken lines) provide an even worse prediction for the six motors.

The notable differences between theoretical and experimental torque/speed curves have been pointed out in the classical literature [1][5]-[8], and are generally associated with space harmonics. A thorough analysis of this outdated topic reveals that torque irregularities are present in practice because the air-gap flux density contains harmonics produced by [1]: (1) amount of mmf in a finite number of slots (winding harmonics), (2) non-uniform air-gap due to stator and rotor slot openings (slot harmonics), and (3) machine saturation. Then, the air-gap mmf and flux density can be expressed as [9]-[11]

$$\begin{aligned} f(x,t) &= \sum_{k=1,3,5} F_k \cdot \cos\big(k(x-\alpha)\big) \cdot i(t) \qquad \left(F_k = \pm\frac{2}{\pi}\frac{N\xi_k}{k}\right) \\ B(x,t) &= \mu_0 \cdot g^{-1}(x, p\theta_{\mathrm{m}}) \cdot \sum_{k=1,3,5} F_k \cdot \cos\big(k(x-\alpha)\big) \cdot i(t), \end{aligned} \tag{3}$$

where k is the harmonic order (including the fundamental) and amplitude F_k depends on the winding arrangement (number of turns N and winding factor for harmonic k, ξ_k). The positive sign in F_k is for the harmonics of order $k = 2n+1$ ($n = 0, 1, 2...$), i.e., $k = 1, 5, 11...$, whereas the negative sign is for the harmonics of order $k = 2n+3$, i.e., $k = 3, 7, 9...$ The air-gap length is no longer a constant but depends on the position angle x and the rotor mechanical angle θ_{m} (p is the number of pole pairs). Only odd harmonics are considered in (3) because the winding arrangement is assumed to be symmetrical about its magnetic axis α.

The flux density harmonics in (3) are translated into torque irregularities (i.e., torque dips and cusps at large slips, also called parasitic torques), which may be of considerable amplitude [1]. It was observed that, for some stator and rotor slot combinations, parasitic torques could seriously impair (or even impede) motor start up. This is known as crawling. Indeed, pronounced irregularities at large slips and in the braking regime (also known as hooks) were reported experimentally [5]-[8]. Some authors tried to explain this behaviour analytically and make rules to prevent its occurrence [1][8].

A priori, the quality of the air-gap field should depend on the motor size and design. However, there are no significant differences between the torque curve shapes of the low and medium size motors of Fig. 1, Fig. 2 and Fig. 3 and those that can be guessed for the large size motors #8 and #9 in Table 1. Although the parasitic torques resulting from (3) can be of asynchronous or synchronous nature [12], no parasitic synchronous torques were detected in the tested motors presented here (also, such torques were not specifically searched for). As a consequence, the paper only focuses on the parasitic asynchronous torques of the tested motors.

The available models to study squirrel-cage motors in the presence of space harmonic effects can be categorized into three groups:

- Accurate electromagnetic models, e.g., finite-element method models. These models are usually chosen in the stage design and require the use of manufacturer confidential data.
- Models which include not only the number of stator turns and rotor bars in slots (winding harmonics), but also air-gap permeance variation (slot harmonics) [1][8]-[15]. The complexity of such models is outside the scope of this paper.
- Simplistic steady-state equivalent circuits, i.e., the chain models in Fig. 5c-d. These models are numerically efficient and provide accurate steady-state torque- and current-slip curves.

This paper focuses on the third type of models. An accurate prediction of their torque and current is required in the next practical cases:

- Calculation of motor starting time, mainly when constant power loads are driven (loads with high starting torque requirement).

- Prediction of stator current consumption and rotor speed stability in case of a large speed drop due to a voltage sag [16].
- Use of aggregated motor models for power system studies.

In this paper, the steady-state torque and current of motors #1, #2 and #3 operating in the braking and motoring regimes are measured, and a set of parameters for the steady-state equivalent circuit (which must be valid for both regimes) is searched for. Two sets of estimated parameters failed in the torque-slip curve prediction. In the first, the classical single- and double-cage models were used whereas in the second, the single-cage chain model, which considers the space harmonics but neglects the skin effect, was employed. Finally, the classical single-cage chain model (which includes both space harmonics and skin effect, and was proposed in the early 60’s [5]-[7][17]) successfully predicts the measured data.

Despite the great number of references to the classical single-cage chain model [1][2][5]-[8][15], few studies in the literature fit this model to measurements, i.e., its ability to predict measured machine behaviour in the presence of space harmonic effects has not been evaluated.

2 Laboratory measurements

The squirrel-cage motors #1, #2 and #3 were tested by the authors in the laboratory whereas motors #4, #5 and #6 were tested by the manufacturer. The tests measured the torque and the stator current at different steady-state operating points (at different speeds). To collect more information, the measured range also included the braking regime (i.e., torque and current were measured from $s = 2$ to $s = 0$) for motors #1 to #3.

Motors #1, #2 and #3 were tested at a reduced voltage of $0.82 \cdot U_N = 328$ V due to source limitations while motors #4, #5 and #6 were tested at $0.57 \cdot U_N = 230$ V. The torque and current measured at a reduced voltage are prorated to the rated voltage to make them comparable:

$$\begin{aligned} T_{\text{prorated}} &= T_{\text{measured}} \left(\frac{U_{\text{N}}}{U_{\text{measured}}} \right)^2 \\ I_{\text{s prorated}} &= I_{\text{s measured}} \frac{U_{\text{N}}}{U_{\text{measured}}} . \end{aligned} \tag{4}$$

The experimental measurements are represented by circles in Fig. 1 and Fig. 2. Strong torque irregularities which may be the cause of disagreement between theoretical and experimental curves, especially if the classical single-cage model is used in the braking regime of Fig. 1, can be observed. The effect varies for the different motors; that is, while in motor #1 torque irregularities are practically inexistent, the remaining five motors exhibit a torque dip at large slips (in the motoring regime). Furthermore, motors #2 and #3 show a pronounced torque increase in the braking regime.

Despite these irregularities, the current-slip curves are very smooth in the six cases. The smooth torque curve of motor #1 makes it possible to fit the measurements by the classical models, as seen in Section 4. On the other hand, the torque curves of the remaining five motors probably require a more complete machine model. Regarding the origin of the torque irregularities in these five motors, the space harmonics are a good candidate after examination of the almost *pathological* torque curves measured in [6][8], where abrupt hooks were caused by the space harmonics due to specific stator and rotor slot combinations.

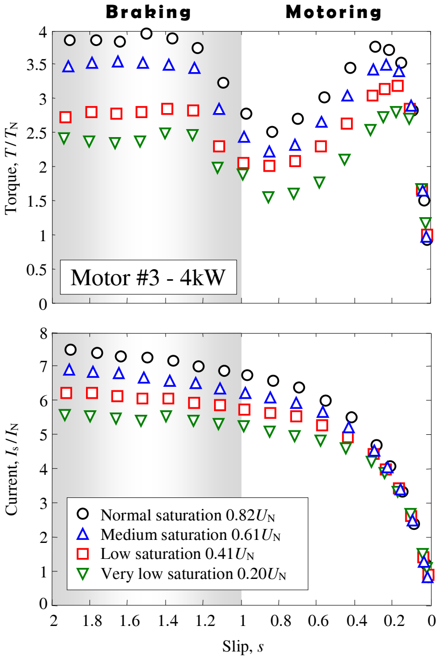

Fig. 4 *Measured torque- and current-slip curves for motor #3 at different voltage levels.*

It is well known that the induction machine inductances saturate. For example, the rotor leakage inductance in machines with closed rotor slots is highly dependent on the current at large slips, whereas the main flux inductance saturates in machines with rotor skewing due to uncompensated mmf at stack end-parts [1]. Therefore, machine saturation could be another reason for these irregularities but this possibility is ruled out in the next subsection.

2.1 Discarding machine saturation

To discard saturation as the origin of the irregularities in Fig. 1, Fig. 2 and Fig. 3, the following laboratory test was made on motor #3. The motor was fed at four voltage levels in the whole speed range in order to obtain the corresponding torque- speed curves. Each voltage level includes the saturation effect at all operating points, including large slip ones, where the current is several times greater than the nominal [18]. By making different tests at a) 0.82 times the nominal voltage U_N, which represents the normal saturation level, b) 0.61 and 0.41 times the nominal voltage, which represent medium saturation levels, and c) 0.20 times the nominal voltage, which characterizes the unsaturated machine, the curves with the (prorated) measurements for motor #3 are obtained and represented in Fig. 4.

Although the curves are slightly different at the different saturation levels, they have a similar shape. Therefore, saturation should not be considered the sole origin of the measured irregularities.

If a full model to simultaneously predict the four tested voltage levels in Fig. 4 were searched for, a model with non-linear reactances should be considered for successful curve fitting [18]. As only the tested voltage level must be fit in this paper (i.e., the tested voltage level in Fig. 1 and Fig. 2), a model with linear reactances is considered from this point in the paper.

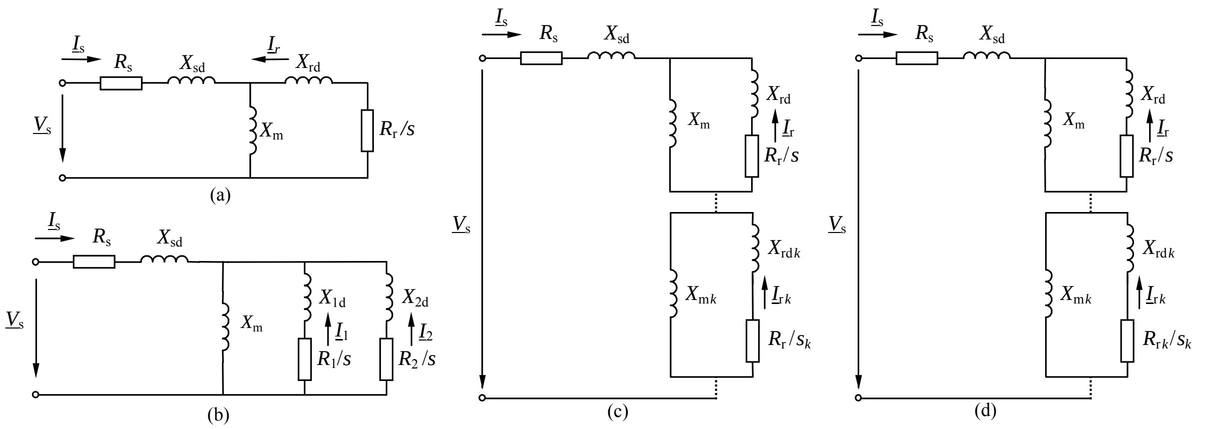

Fig. 5 (a) Single-cage model without space harmonic effects, (b) double-cage model without space harmonic effects, (c) single-cage chain model without skin effect, and (d) single-cage chain model with skin effect.

2.2 Measured stator current harmonics

Instantaneous stator currents measured in the tests of Fig. 1 were almost sinusoidal in all cases. It is worth noting that these measurements are in full agreement with the results in [15], where detailed simulations show that, unlike their obvious influence on the torque, the impact of space harmonics on stator currents is almost negligible. The space harmonic models used in this paper (chain models in Fig. 5c-d) are based on the assumption that the stator currents are purely sinusoidal.

3 Models for predicting the measured behaviour

Once motor saturation is ruled out, an attempt was made to fit the measured machine behaviour with the three types of models in Sections 4, 5 and 6:

(1) the single- and double-cage models without space harmonic effects in Fig. 5a-b, which consider sinusoidal air-gap flux density distribution. These models are also called ‘classical models’ in this paper;

(2) the single-cage chain model in Fig. 5c, which considers space harmonics due to non-sinusoidally distributed windings and uniform air-gap but neglects the skin effect, and

(3) the single-cage chain model in Fig. 5d, which takes into account both space harmonics and skin effect.

The chain models are based on the common assumption that the squirrel-cage rotor reacts to all harmonic fluxes in the same way as to the fundamental, thus leading to a parasitic torque-slip curve for each harmonic [1][6].

4 Single- and double-cage models without space harmonic effects

Fig. 5a-b shows the equivalent circuits for the single- and double-cage models without space harmonic effects, i.e., the classical models. Their torque is calculated with the following equations:

$$T(s)=\frac{3p}{\omega_s}\left(\frac{R_r}{s}I_r^2\right)\quad,\quad T(s)=\frac{3p}{\omega_s}\left(\frac{R_1}{s}I_1^2+\frac{R_2}{s}I_2^2\right),\tag{5}$$

where $s=\dfrac{\omega_s-p\omega_m}{\omega_s}$ is the slip at the fundamental frequency and p is the number of pole pairs.

4.1 Parameter estimation

As the stator resistance R_s was measured off-line, only three functional relationships can be estimated between the remaining four unknown electrical parameters of the single-cage model in Fig. 5a [19]. As a solution, the restriction $X_{sd} = X_{rd}$ is arbitrarily chosen in this study. The estimation procedure is based on the following data and unknowns:

$$\begin{array}{ll} \multicolumn{2}{l}{\underline{\text{Single-cage model without space harmonic effects}}} \\ \triangleright \text{ Unknowns:} & X_{sd}, X_m, R_r \\ \triangleright \text{ Data:} & R_s \\ \triangleright \text{ Restriction:} & X_{rd} = X_{sd} \\ \triangleright \text{ Data to fit:} & \text{Tests in Figs. 1 and 2.} \end{array} \tag{6}$$

Regarding the double-cage model in Fig. 5b, it has six unknown electrical parameters as R_s has been measured. Since only five functional relationships between these parameters are independent [19], the restriction $X_{sd} = X_{2d}$ is arbitrarily chosen in this paper. The estimation procedure is based on the following data and unknowns:

$$\begin{array}{ll} \multicolumn{2}{l}{\underline{\text{Double-cage model without space harmonic effects}}} \\ \triangleright \text{ Unknowns:} & X_{sd}, X_m, R_1, X_{1d}, R_2 \\ \triangleright \text{ Data:} & R_s \\ \triangleright \text{ Restriction:} & X_{2d} = X_{sd} \\ \triangleright \text{ Data to fit:} & \text{Tests in Figs. 1 and 2.} \end{array} \tag{7}$$

4.2 Least-squares algorithm for parameter estimation

In this paper, the model parameters are estimated with a MATLAB built-in function for least-squares fit [20]. The errors between estimated and measured data are given in values relative to the measured values:

$$\varepsilon_{xi} = \left| \frac{x_{i\ \text{estimated}} - x_{i\ \text{measured}}}{x_{i\ \text{measured}}} \right|. \tag{8}$$

The error function to be optimized is a column vector [**F**] composed of the following scalar error functions, where the weight given to each point (w_i) can be modified if needed:

$$[\mathbf{F}] = \begin{bmatrix} F_1 \\ F_2 \end{bmatrix} \quad \text{where: } F_1 = \frac{1}{N} \sum_{i=1}^{N} w_i\, \varepsilon_{\text{torque } i} \qquad F_2 = \frac{1}{N} \sum_{i=1}^{N} w_i\, \varepsilon_{\text{current } i} \qquad w_i = 1. \tag{9}$$

The least-squares algorithm minimizes the 2-norm residual error:

$$\text{Residual error}\,(\%) = \|\mathbf{F}\|_2 = 100 \cdot \left(\sum_{i=1}^{2} F_i^2 \right)^{1/2}. \tag{10}$$

To avoid negative values of the estimated parameters, it is recommended to force all parameters to be always positive [19].

Table 2 Estimated parameters in pu ($S_B = P_N$, $U_B = U_N$, $Z_B = U_B^2 / S_B$) for the single- and double-cage models without space harmonic effects

	Single-cage model without space harmonic effects					Double-cage model without space harmonic effects						
	r_s	x_{sd}	x_m	r_r	x_{rd}	r_s	x_{sd}	x_m	r_1	x_{1d}	r_2	x_{2d}
Motor #1	0.0422	0.0749	1.0617	0.0313	0.0749	0.0422	0.0595	1.0771	0.0371	0.1236	0.2430	0.0595
Motor #2	0.0350	0.0612	1.0328	0.0218	0.0612	0.0350	0.0409	1.0532	0.0253	0.1060	0.2153	0.0409
Motor #3	0.0244	0.0402	1.2767	0.0253	0.0402	0.0244	0.0244	0.0250	1.2103	0.0241	0.0836	0.1781
Motor #4	0.0422	0.0749	1.0617	0.0313	0.0749	0.0422	0.0595	1.0771	0.0371	0.1236	0.2430	0.0595
Motor #5	0.0350	0.0612	1.0328	0.0218	0.0612	0.0350	0.0409	1.0532	0.0253	0.1060	0.2153	0.0409
Motor #6	0.0244	0.0402	1.2767	0.0253	0.0402	0.0244	0.0244	0.0250	1.2103	0.0241	0.0836	0.1781

4.3 Estimation results analysis

The parameters estimated for the classical models of motors #1 to #6 are given in Table 2. The predicted torque- and current-slip curves are calculated from these parameters and plotted in Fig. 1 and Fig. 2 (single-cage: broken line; double-cage: solid line).

Analysis of both figures shows that the classical single-cage model cannot accurately predict the behaviour of any of the six motors.

The classical double-cage model can be considered adequate only for motor #1 given that, although the torque-slip curve is very smooth and provides better results, it also fails to predict the torque of the remaining five motors.

It is worth noting that the torque predictions in the motoring regime (from $s = 1$ to $s = 0$) for motors #2 and #3 can lead to the wrong conclusion that the classical single-cage models are more accurate in such a speed range. This is erroneous as the classical double-cage models in Fig. 1 provide better predictions in the whole speed range (i.e., from $s = 2$ to $s = 0$).

Although motors #7, #8 and #9 were not tested, the low values of the minimum torque compared to the starting torque (T_{MIN}/T_{ST}) in Table 1 suggest that the classical single- and double-cage models would fail in the torque prediction.

5 Single-cage chain model without skin effect

Fig. 5c illustrates the steady-state equivalent circuit for the three-phase induction machine with non-sinusoidally distributed windings and uniform air-gap. The model considers a single-cage for the rotor and neglects the skin effect. As can be seen, the circuit contains a rotor subcircuit for any considered space harmonic, resulting into a chain model. As the skin effect is neglected, the rotor resistance is identical for all subcircuits, and the leakage reactances $X_{rd\ k}$ are rigidly related to X_m, $X_{m\ k}$ and X_{rd}. Appendix 1 contains a detailed deduction of the model equations because no complete demonstration was found in the literature.

The authors tried to fit the model to the measurements of Fig. 1. As the adjustment was unsuccessful in all cases, it can be concluded that the model is unable to predict the measured squirrel-cage torque irregularities in Fig. 1. As a result, it seems apparent that the skin effect must be included in the space harmonic model.

6 Single-cage chain model with skin effect

Fig. 5d shows the steady-state equivalent circuit for the three-phase induction machine which includes the space harmonics and the skin effect [1][2]. This model maintains the rotor subcircuit topology in Fig. 5c. However, the skin effect consideration results in variable rotor resistances and reactances $X_{\mathrm{rd}\,k}$ for any considered space harmonic. The model is also valid for non-uniform air-gap (slot harmonics).

In this model, the total and harmonic torques are calculated as follows:

$$\begin{aligned} & T(s) = \sum_{k=1,5,7\ldots} T_k(s) = \sum_{k=1,5,7\ldots} \pm k \frac{3p}{\omega_{\mathrm{s}}} \left(\frac{R_{\mathrm{r}k}}{s_k} I_{\mathrm{r}k}^2 \right) \\ & \text{being:} \quad s_k = \frac{\omega_{\mathrm{s}} - (\pm k p \omega_{\mathrm{m}})}{\omega_{\mathrm{s}}} = 1 - (\pm k(1-s)) \\ & (k = 1,\ 5,\ 7,\ 11\ldots), \end{aligned} \tag{11}$$

where ± must be interpreted as follows:

- ▷ the positive sign is for the *forward* harmonics: the fundamental ($k = 1$) and the harmonics of order $k = 7$, 13... (i.e., $k = 6n + 1$, where $n = 0, 1, 2\ldots$).
- ▷ the negative sign is for the *backward* harmonics: the harmonics of order $k = 5$, 11... (i.e., $k = 6n + 5$, where $n = 0, 1, 2\ldots$).

6.1 Parameter estimation

The 5th, 7th and 11th harmonics are chosen for curve fitting. It must be remembered that the 7th harmonic flux travels forward (in the direction of the fundamental field) at a sub-synchronous speed of $(\omega_{\mathrm{s}}/p)/7$ while the 5th and 11th travel backward at sub-synchronous speeds of $(\omega_{\mathrm{s}}/p)/5$ and $(\omega_{\mathrm{s}}/p)/11$. The estimation procedure is based on the following data and unknowns:

$$\begin{array}{ll} \multicolumn{2}{l}{\underline{\text{Single-cage chain model with skin effect}}} \\ \triangleright\ \text{Unknowns:} & X_{\mathrm{sd}}, X_{\mathrm{m}}, R_{\mathrm{r}} \\ & X_{\mathrm{m}k}, R_{\mathrm{r}k}, X_{\mathrm{rd}k} \quad (k = 5, 7, 11) \\ \triangleright\ \text{Data:} & R_{\mathrm{s}} \\ \triangleright\ \text{Restriction:} & X_{\mathrm{rd}} = X_{\mathrm{sd}} \\ \triangleright\ \text{Data to fit:} & \text{Test in Fig. 1}. \end{array} \tag{12}$$

Note that the arbitrary restriction $X_{\mathrm{sd}} = X_{\mathrm{rd}}$ is again imposed on the parameters related to the fundamental flux.

6.2 Estimation results analysis

The parameters estimated for motors #1, #2 and #3 are given in Table 3. It is worth noting that, while the estimation for motors #1 and #3 was very straightforward, in the case of motor #2 it was necessary to modify the weights given to the different points, w_i.

The predicted curves are calculated from the parameters of Table 3 and plotted in Fig. 6. This figure also contains the contribution of the harmonic torques, whose zero-crossing occurs at $s = 1 - (\pm 1/k) = 1 + 1/5$, $1 - 1/7$, $1 + 1/11$, as can be deduced from (11) by imposing $s_k = 0$.

Table 3 Single-cage chain model with skin effect: estimated parameters in pu ($S_B = P_N$, $U_B = U_N$, $Z_B = U_B^2 / S_B$)

		Motor #1	Motor #2	Motor #3
	r_s	0.0422	0.0350	0.0244
	$x_{sd} = x_{rd}$	0.0597	0.3701	0.0257
	x_m	0.9288	1.2104	1.4292
	r_r	0.0364	0.0349	0.0256
5th	$x_{m\,(5)}$	0.0012	0.0071	0.0102
	$r_{r\,(5)}$	0.1781	0.1197	0.3015
	$x_{rd\,(5)}$	0.1909	0.0009	0.0180
7th	$x_{m\,(7)}$	0.0075	0.0069	0.0053
	$r_{r\,(7)}$	0.0784	0.1203	0.0698
	$x_{rd\,(7)}$	0.0024	0.0081	0.0039
11th	$x_{m\,(11)}$	0.0001	0.0179	0.0102
	$r_{r\,(11)}$	0.1101	0.4988	0.4302
	$x_{rd\,(11)}$	0.1146	0.3202	0.0091

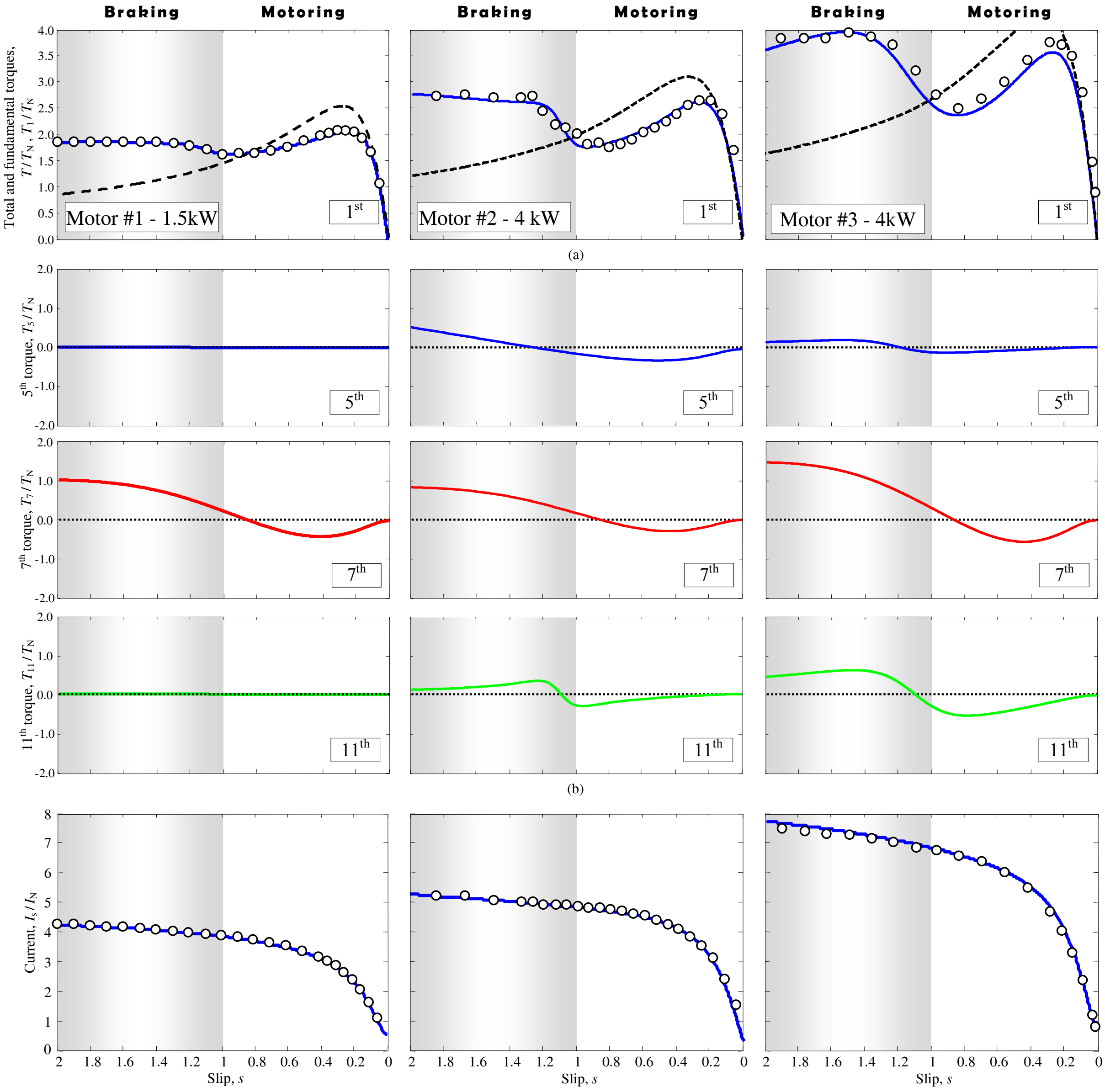

(a)

(b)

(c)

Fig. 6 Prediction of the single-cage chain model with skin effect for the three tested small size motors: (a) the total (solid line) and fundamental torques (broken line) (b) harmonic torques, and (c) total current.

Table 4 Average and maximum torque- and current-slip errors for the three models in all six tested motors

	Single-cage model without space harmonic effects				Double-cage model without space harmonic effects				Single-cage chain model with skin effect			
	Torque error		Current error		Torque error		Current error		Torque error		Current error	
	Av.	Max.	Av.	Max.	Av.	Max.	Av.	Max.	Av.	Max.	Av.	Max.
Motor #1	34.82	70.94	8.04	15.31	6.14	20.98	7.43	11.06	2.43	5.75	2.15	5.87
Motor #2	36.33	78.99	3.69	8.02	10.64	28.28	3.12	6.59	2.63	8.63	3.09	8.34
Motor #3	35.55	72.84	2.79	4.91	24.71	67.41	5.39	18.82	4.05	10.95	2.12	6.68
Motor #4	24.03	72.03	13.76	27.91	17.80	55.42	11.06	19.52				
Motor #5	25.16	66.42	8.71	24.69	18.53	44.70	6.56	14.81				
Motor #6	30.51	76.43	6.59	22.39	5.32	25.51	7.22	14.46				

Note that the harmonic torque curves are not symmetrical about the horizontal axis, just like in the classical models in Fig. 5a-b (the torque-slip curve for motor operation is not identical to that for generator operation). This asymmetry is particularly apparent in the 7th harmonic torques of the three motors because there is a significant torque increase in the braking regime whereas the impact at rated slip is low.

The fit obtained for motor #1 in Fig. 6 is slightly better than that obtained with the classical double-cage model in Fig. 1. The fit for motors #2 and #3 is also excellent, as the estimated parameters accurately predict the pronounced torque irregularities.

The number of space harmonics is chosen a priori. Considering the results in Fig. 6, the 5th harmonic could be discarded a posteriori for motors #1 and #3, and the 11th for motors #1 and #2 without significant loss of accuracy.

7 Models comparison and summary

The accuracy of the classical single- and double-cage models and the single-cage chain model with skin effect to predict the measured curves in the three motors is quantified in Table 4. The average and maximum errors in torque and stator versus slip curves are shown in the table. These errors confirm the inappropriateness of the classical single- and double-cage models for torque prediction (average errors for all motors are 31% and 14%, respectively), whereas the single-cage chain model with skin effect provides by far the most accurate predictions (average error for all motors is 3%). Regarding the current predictions, the differences among the three models are less pronounced (average errors for all motors are 7%, 7% and 2%, respectively).

Finally, Table 5 summarizes with a check mark (✓) or a cross mark (×) the ability or inability of each model to predict the torque curves. The classical single- and double-cage models and the single-cage chain model without skin effect are unable to simultaneously predict space harmonics and skin effect. On the contrary, the single-cage chain model which considers the skin effect provides accurate predictions.

Table 5 Models summary

		Skin effect	Space harmonics
Fig. 5a	Single-cage model without space harmonic effects (classical model)	×	×
Fig. 5b	Double-cage model without space harmonic effects (classical model)	✓	×
Fig. 5c	Single-cage chain model without skin effect	×	✓
Fig. 5d	Single-cage chain model with skin effect	✓	✓

8 Conclusions

The paper shows the measured torque- and current-slip curves of six squirrel-cage induction motors. Five units exhibit apparent torque irregularities caused by space harmonics. For completeness, the measured range was extended to the braking regime ($s = 2$ to $s = 1$) for three of the motors. The measured data are successfully fit by the following models: (1) the classical single- and double-cage models, (2) the single-cage chain model which considers space harmonics effects but neglects the skin effect, and (3) the single-cage chain model which takes into account both space harmonics and skin effects.

It is concluded that the smooth torque curves predicted by the classical models do not fit the measured curves when space harmonic effects are apparent. The single-cage chain model which neglects the skin effect also fails in the torque prediction despite considering space harmonics effects. On the contrary, the single-cage chain model which takes into account both space harmonics and skin effects exhibits excellent agreement with experimental data.

9 Appendix 1: single-cage chain model without skin effect

In this appendix, a simplistic dynamic model in space vector variables for an induction machine with non-sinusoidally distributed windings, uniform air-gap and without skin effect is derived. By imposing electrical and mechanical steady-state, and assuming that a sinusoidal current source supplies the stator, the chain equivalent circuit in Fig. 5c is obtained. This circuit can be considered as a particular case of the more general chain model in Fig. 5d, which considers the space harmonics due to the skin effect and non-uniform air-gap. Because of its low computational burden, the model derived in this appendix can be used as a simulation tool to provide useful, qualitative dynamic and steady-state results.

9.1 Model assumptions

The following assumptions about a three-phase induction machine are made:

- Ideal magnetic circuit (negligible saturation and infinite relative magnetic permeability).
- Uniform air-gap.
- Three identical stator and rotor windings having constant parameters (due to skin effect on the rotor windings) and symmetrical arrangement about their magnetic axes (located at α, $\alpha+2\pi/3$ and $\alpha-2\pi/3$).
- Constant leakage flux inductances.

The mutual inductance m_{ab} of two windings a and b whose magnetic symmetry axes are inclined at α_{a} and α_{b} electrical degrees, respectively, is calculated by integration of the flux linkage of winding a, characterized by (3), with winding b. Assuming uniform air-gap, the resulting expression is [9]-[11]

$$\begin{aligned} m_{\mathrm{ab}} &= \sum_{k=1,3,5} \mu_{\mathrm{o}} g^{-1} r b_{\mathrm{e}} \frac{4}{\pi} \frac{\left(N_{\mathrm{a}}\xi_{\mathrm{a}k}\right)\left(N_{\mathrm{b}}\xi_{\mathrm{b}k}\right)}{k^{2}} \cos\left(k\left(\alpha_{\mathrm{a}}-\alpha_{\mathrm{b}}\right)\right) \\ &= \sum_{k=1,3,5} m_{\mathrm{ab}k} \cos\left(k\left(\alpha_{\mathrm{a}}-\alpha_{\mathrm{b}}\right)\right), \end{aligned} \tag{13}$$

where r is the average radius and b_{e} is the stack length. The calculation of the self-inductance of winding a must also consider the leakage flux, i.e., the leakage flux inductance l_{ad} must be added to (13): $l_{\mathrm{a}} = m_{\mathrm{aa}} + l_{\mathrm{ad}}$.

The inductance calculation in (13) is simplified because the stator and rotor winding arrangements are identical ($\xi_{\mathrm{s}\,k} = \xi_{\mathrm{r}\,k} = \xi_k$). Further simplification is obtained by reducing the rotor parameters to the stator ($N_\mathrm{s} = N_\mathrm{r} = N$):

$$\begin{aligned} m_\mathrm{ab} &= \sum_{k=1,3,5} \mu_\mathrm{o} g^{-1} r b_\mathrm{e} \frac{4}{\pi} \frac{\left(N\xi_k\right)^2}{k^2} \cos\left(k\left(\alpha_\mathrm{a} - \alpha_\mathrm{b}\right)\right) \\ &= \sum_{k=1,3,5} m_k \cos\left(k\left(\alpha_\mathrm{a} - \alpha_\mathrm{b}\right)\right) \qquad \left(m_k = m_1 \frac{\left(\xi_k/\xi_1\right)^2}{k^2}\right). \end{aligned} \tag{14}$$

Note that concentrated windings (square-wave mmfs) lead to the largest space harmonic content. In this case, the maximum value for m_k is obtained as $\xi_k = 1$, resulting in $m_k = m_1/k^2$.

9.2 Dynamic model equations in space vector variables

The *abc* phase model for the induction machine is given by

$$\begin{aligned} &[\mathbf{v}] = [\mathbf{R}][\mathbf{i}] + \frac{\mathrm{d}}{\mathrm{d}t}[\boldsymbol{\lambda}] \qquad [\boldsymbol{\lambda}] = \left[\mathbf{M}(\theta)\right][\mathbf{i}] \\ &\theta = p\theta_\mathrm{m} + \theta_0 \\ &T(t) = \frac{1}{2}[\mathbf{i}]^\mathrm{t} \frac{\partial\left[\mathbf{M}(\theta)\right]}{\partial\theta_\mathrm{m}}[\mathbf{i}] = p\frac{1}{2}[\mathbf{i}]^\mathrm{t} \frac{\partial\left[\mathbf{M}(\theta)\right]}{\partial\theta}[\mathbf{i}], \end{aligned} \tag{15}$$

where θ is the rotor mechanical angle in electrical degrees and θ_0 is its value at instant $t = 0$ s. The inductance matrix is defined as

$$\left[\mathbf{M}(\theta)\right] = \begin{bmatrix} \mathbf{M}_\mathrm{s} & \mathbf{M}_\mathrm{sr} \\ \mathbf{M}_\mathrm{rs} & \mathbf{M}_\mathrm{r} \end{bmatrix}. \tag{16}$$

This matrix contains the winding inductances

$$\begin{aligned} &\left[\mathbf{M}_\mathrm{s}(k)\right] = l_\mathrm{sd} \begin{bmatrix} 1 & 0 & 0 \\ 0 & 1 & 0 \\ 0 & 0 & 1 \end{bmatrix} + \sum_{k=1,3,5} m_k \begin{bmatrix} 1 & -1/2 & -1/2 \\ -1/2 & 1 & -1/2 \\ -1/2 & -1/2 & 1 \end{bmatrix} \\ &\left[\mathbf{M}_\mathrm{r}(k)\right] = l_\mathrm{rd} \begin{bmatrix} 1 & 0 & 0 \\ 0 & 1 & 0 \\ 0 & 0 & 1 \end{bmatrix} + \sum_{k=1,3,5} m_k \begin{bmatrix} 1 & -1/2 & -1/2 \\ -1/2 & 1 & -1/2 \\ -1/2 & -1/2 & 1 \end{bmatrix} \\ &\left[\mathbf{M}_\mathrm{sr}(k,\theta)\right] = \left[\mathbf{M}_\mathrm{rs}(k,\theta)\right]^\mathrm{t} \\ &= \sum_{k=1,3,5} m_k \begin{bmatrix} \cos(k\theta) & \cos\left(k\left(\theta + \frac{2\pi}{3}\right)\right) & \cos\left(k\left(\theta - \frac{2\pi}{3}\right)\right) \\ \cos\left(k\left(\theta - \frac{2\pi}{3}\right)\right) & \cos(k\theta) & \cos\left(k\left(\theta + \frac{2\pi}{3}\right)\right) \\ \cos\left(k\left(\theta + \frac{2\pi}{3}\right)\right) & \cos\left(k\left(\theta - \frac{2\pi}{3}\right)\right) & \cos(k\theta) \end{bmatrix}, \end{aligned} \tag{17}$$

where l_sd and l_rd are the stator and rotor leakage inductances, and m_k is given by (14).

The *abc* variables are transformed into the 0FB variables by the complex rotating transformation [**T**] or forward-backward transformation (abbreviated as FB-transformation) [21] expressed in the stationary reference frame

$$[\mathbf{x}_\mathrm{T}]=[\mathbf{T}][\mathbf{x}] \quad \rightarrow \quad \begin{bmatrix} x_0 \\ x_\mathrm{F} \\ x_\mathrm{B} \end{bmatrix} = \frac{1}{\sqrt{3}} \begin{bmatrix} 1 & 1 & 1 \\ 1 & \mathrm{a} & \mathrm{a}^2 \\ 1 & \mathrm{a}^2 & \mathrm{a} \end{bmatrix} \begin{bmatrix} x_\mathrm{a}(t) \\ x_\mathrm{b}(t) \\ x_\mathrm{c}(t) \end{bmatrix}, \\ \left(\text{being } [\mathbf{T}]^{-1}=\left[\mathbf{T}^*\right]^\mathrm{t}\right) \tag{18}$$

where 0 is the zero-sequence component, and F and B are the forward and backward components, which are complex conjugate. Note that matrix [**T**] in (18) is the Fortescue matrix, which is used for the symmetrical component transformation. The forward component of (18) is also known in the literature as the space vector, the spatial vector, or the space phasor of the *abc* phase quantities.

The electrical equations of (15) are expressed in transformed variables as

$$\begin{gathered} [\mathbf{v}_\mathrm{T}]=[\mathbf{R}][\mathbf{i}_\mathrm{T}]+\frac{\mathrm{d}}{\mathrm{dt}}[\boldsymbol{\lambda}_\mathrm{T}] \qquad [\boldsymbol{\lambda}_\mathrm{T}]=\left[\mathbf{M}_\mathrm{T}(\theta)\right][\mathbf{i}_\mathrm{T}] \\ \left[\mathbf{M}_\mathrm{T}(\theta)\right]=[\mathbf{T}_\mathrm{C}]\left[\mathbf{M}(\theta)\right][\mathbf{T}_\mathrm{C}]^{-1}, \end{gathered} \tag{19}$$

where $[\mathbf{T}_\mathrm{C}]$ is the complete transformation matrix

$$[\mathbf{T}_\mathrm{C}] = \begin{bmatrix} \mathbf{T} & \mathbf{0} \\ \mathbf{0} & \mathbf{T} \end{bmatrix}. \tag{20}$$

The electromagnetic torque expressed in transformed variables is calculated as

$$T(t)=p\frac{1}{2}\left[\mathbf{i}_\mathrm{T}^*\right]^\mathrm{t}\frac{\partial}{\partial\theta}\left\{\left[\mathbf{M}_\mathrm{T}(\theta)\right]\right\}[\mathbf{i}_\mathrm{T}]. \tag{21}$$

The stator and rotor zero-sequence equations in (19) are decoupled from the remaining equations. Furthermore, the forward and backward equations of (19) are complex conjugate. Thus, machine behaviour can be expressed with the zero-sequence and forward equations only, and using the 0 and F variables:

$$\begin{aligned} &\boxed{k=6n+3 \quad (n=0,1,2...)} \\ &v_\mathrm{s0}=R_\mathrm{s}i_\mathrm{s0}+\frac{\mathrm{d}}{\mathrm{dt}}\left\{\left(L_\mathrm{sd}+\sum_{k=3,9,15}2M_k\right)i_\mathrm{s0}\right\} \\ &v_\mathrm{r0}=R_\mathrm{r}i_\mathrm{r0}+\frac{\mathrm{d}}{\mathrm{dt}}\left\{\left(L_\mathrm{rd}+\sum_{k=3,9,15}2M_k\right)i_\mathrm{r0}\right\} \\ &\boxed{\begin{array}{l} k=6n+1 \text{ (positive sign) and } k=6n+5 \text{ (negative sign)} \\ (n=0,1,2...) \end{array}} \\ &\begin{bmatrix} v_\mathrm{sF} \\ v_\mathrm{rF} \end{bmatrix} = \begin{bmatrix} R_\mathrm{s} & 0 \\ 0 & R_\mathrm{r} \end{bmatrix} \begin{bmatrix} i_\mathrm{sF} \\ i_\mathrm{rF} \end{bmatrix} \\ &\qquad +\frac{\mathrm{d}}{\mathrm{dt}}\left\{\begin{bmatrix} L_\mathrm{sd}+\sum\limits_{k=1,5,7}M_k & \sum\limits_{k=1,5,7}M_k\mathrm{e}^{\pm jk\theta} \\ \sum\limits_{k=1,5,7}M_k\mathrm{e}^{-(\pm jk\theta)} & L_\mathrm{rd}+\sum\limits_{k=1,5,7}M_k \end{bmatrix} \begin{bmatrix} i_\mathrm{sF} \\ i_\mathrm{rF} \end{bmatrix}\right\}, \end{aligned} \tag{22}$$

where the following change of variables is made:

$$L_\mathrm{sd}=l_\mathrm{sd}, \quad L_\mathrm{rd}=l_\mathrm{rd}, \quad M=\frac{3}{2}m_1, \quad M_k=\frac{3}{2}m_k. \tag{23}$$

In (22) the writing of the equations depends on the order of the harmonic inductances M_k:

The zero-sequence equations only depend on the harmonic inductances of order k = 3, 9, 15... (i.e., $k = 6n+3$, where n = 0, 1, 2...). These harmonics are called *zero-sequence* harmonics.

The positive sign in the forward equations is for the fundamental ($k = 1$) and harmonic inductances of order $k = 7, 13...$, (i.e., $k = 6n+1$, where $n = 0, 1, 2...$). These harmonics are called *forward* harmonics as fluxes of this order travel forward (in the direction of the fundamental field) at sub-synchronous speeds of $(\omega_s/p)/k$.

The negative sign in the forward equations is for the harmonic inductances of order $k = 5, 11...$ (i.e., $k = 6n+5$, where $n = 0, 1, 2...$). These harmonics are called *backward* harmonics as fluxes of this order travel backward (in the direction of the fundamental field) at sub-synchronous speeds of $(\omega_s/p)/k$.

And the torque with only the F variables is

$$\begin{aligned} T(t) &= p\,\mathrm{Re}\left(\begin{bmatrix} i_{\mathrm{sF}}^{*} & i_{\mathrm{rF}}^{*} \end{bmatrix} \frac{\partial}{\partial\theta}\left\{ \left[\mathbf{M}_{\mathbf{TF}}(\theta) \right] \right\} \begin{bmatrix} i_{\mathrm{sF}} \\ i_{\mathrm{rF}} \end{bmatrix} \right) \\ &= p2\,\mathrm{Im}\left(i_{\mathrm{sF}} i_{\mathrm{rF}}^{*} \sum_{k=1,5,7} \pm k M_k \mathrm{e}^{-(\pm \mathrm{j}k\theta)} \right), \end{aligned} \tag{24}$$

where $[\mathbf{M_{TF}}(\theta)]$ is composed of the F elements of matrix $[\mathbf{M_T}(\theta)]$.

9.3 Steady-state equivalent circuit

The steady-state closed-form solution of the previous model is cumbersome because the spectrum of the stator and rotor currents is infinite even if only one harmonic in M_k is considered (assuming the stator is supplied by a sinusoidal voltage source). A steady-state model with truncation of stator and rotor currents was obtained but it is not included here for brevity purposes [22].

A more useful approximate steady-state solution is found if stator windings are assumed to be supplied by a sinusoidal current source of pulsation ω_s, rms amplitude I_{s1}, and phase *a* angle φ_{Is1}. According to (18), the forward stator current is

$$i_{\mathrm{sF}} = i_{\mathrm{sF}1} = \sqrt{3/2}\cdot I_{\mathrm{s}1}\,\mathrm{e}^{\mathrm{j}(\omega_s t + \varphi_{\mathrm{Is}1})} = \sqrt{3/2}\cdot \underline{I}_{\mathrm{s}1}\,\mathrm{e}^{\mathrm{j}\omega_s t}, \tag{25}$$

where $\underline{I}_{s1}$ is the phasor of phase *a*. Let us also assume that the harmonic content of v_{sF} can be neglected:

$$v_{\mathrm{sF}} \approx v_{\mathrm{sF}1} = \sqrt{3/2}\cdot V_{\mathrm{s}1}\,\mathrm{e}^{\mathrm{j}(\omega_s t + \varphi_{\mathrm{Vs}1})} = \sqrt{3/2}\cdot \underline{V}_{\mathrm{s}1}\,\mathrm{e}^{\mathrm{j}\omega_s t}. \tag{26}$$

Then, the analysis of the forward stator equation in (22) indicates the frequencies in i_{rF}. As the term $\frac{\mathrm{d}}{\mathrm{d}t}\left\{\left(L_{\mathrm{sd}} + \sum_{k=1,5,7} M_k\right) i_{\mathrm{sF}1}\right\}$ pulsates at ω_s, then the term $\frac{\mathrm{d}}{\mathrm{d}t}\left\{\left(\sum_{k=1,5,7} M_k \mathrm{e}^{\pm \mathrm{j}k\theta}\right) i_{\mathrm{rF}}\right\}$ also pulsates at ω_s, and the rotor current i_{rF} pulsates at $\left(\omega_s t - (\pm k\theta)\right)/t$. Thus,

$$\begin{aligned} i_{\mathrm{rF}} &= \sum_{k=1,5,7} i_{\mathrm{rF}\,k} = \sum_{k=1,5,7} \sqrt{3/2}\cdot I_{\mathrm{r}\,k}\,\mathrm{e}^{\mathrm{j}(\omega_s t - (\pm k\theta) + \varphi_{\mathrm{Ir}\,k})} \\ &= \sqrt{3/2}\cdot \underline{I}_{\mathrm{r}\,k}\,\mathrm{e}^{\mathrm{j}(\omega_s t - (\pm k\theta))}. \end{aligned} \tag{27}$$

By replacing (25), (26) and (27) in the forward equations of (22), dividing the stator equation by $\sqrt{3/2}\cdot\mathrm{e}^{\mathrm{j}\omega_s t}$ and the rotor equations by $s_k\sqrt{3/2}\cdot\mathrm{e}^{\mathrm{j}(\omega_s t - (\pm k\theta))}$, and using that $\theta = p\omega_m t + \theta_0$, the following phasor equations are obtained:

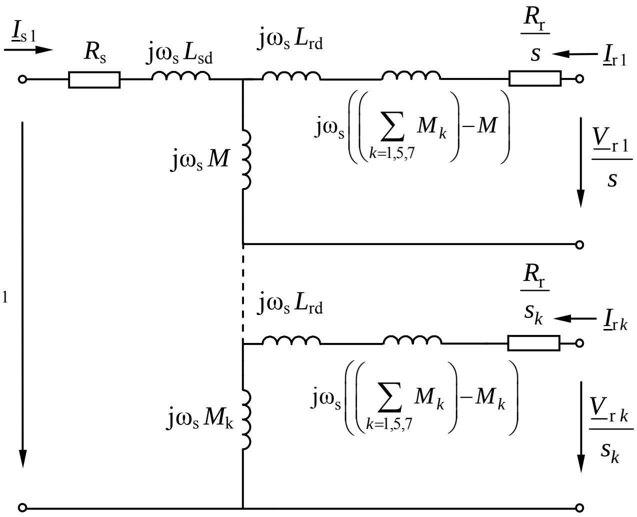

Fig. 7 *Single-cage chain model for the induction machine with non-sinusoidally distributed windings, uniform air-gap and without skin effect. The model assumes that the stator is supplied by a purely sinusoidal current source.*

$$\begin{aligned}
&\underline{V}_{s1} = R_s\underline{I}_{s1} + j\omega_s L_{sd}\underline{I}_{s1} + j\omega_s \sum_{k=1,5,7}\left(M_k\left(\underline{I}_{s1}+\underline{I}_{rk}\right)\right)\\
&\frac{\underline{V}_{rk}}{s_k} = \frac{R_r}{s_k}\underline{I}_{rk} + j\omega_s\left(L_{rd} + \left(\sum_{k=1,5,7} M_k\right) - M_k\right)\underline{I}_{rk}\\
&\qquad + j\omega_s M_k\left(\underline{I}_{s1}+\underline{I}_{rk}\right)\\
&\text{where: }\; s_k = \frac{\omega_s - \left(\pm kp\omega_m\right)}{\omega_s} = 1-\left(\pm k\left(1-s\right)\right)\\
&\left(k = 1,\ 5,\ 7,\ 11...\right).
\end{aligned} \tag{28}$$

These equations can be expressed with the steady-state equivalent circuit in Fig. 7, where the average torque is calculated as

$$\begin{aligned}
T\left(s\right) &= \left\langle T\left(t\right)\right\rangle = 3p\,\mathrm{Im}\left\{\sum_{k=1,5,7} \pm kM_k\underline{I}_{s1}\underline{I}^*_{rk}\right\}\\
&= \sum_{k=1,5,7} \pm k\frac{3p}{\omega_s}\left(\frac{R_r}{s_k}I^2_{rk}\right).
\end{aligned} \tag{29}$$

The circuit in Fig. 7 leads to the chain model in Fig. 5c if the following changes are made: (1) rotor windings are short-circuited (i.e., $\underline{V}_{r1} = \underline{V}_{rk} = 0$), and (2) the two leakage inductances of the rotor subcircuits are substituted by a total rotor leakage inductance (note that the inductance $\left(\sum_{k=1,5,7} M_k\right) - M_k$ can be considered a leakage inductance).

9.4 Dynamic and steady-state model simulation

In order to illustrate the model behaviour, the induction motor of Table 6 is simulated. The parameters of the classical single-cage model are given in this table. A 7th space harmonic is included in the model by considering inductance M_7. The space harmonic amplitude is exaggerated to equal that of a concentrated winding (square-wave mmf): $M_7 = M/49$. Two simulations are performed: the stator is supplied by a voltage source or by a current source.

Table 6 Simulated induction motor parameters in pu ($S_B = P_N$, $U_B = U_N$, $Z_B = U_B^2 / S_B$)

P_N (kW)	U_N (V)	f_N (Hz)	PF_N	ω_N (r/min)	η_N (%)	T_{MAX}/T_N	T_{ST}/T_N	I_{ST}/I_N
2.2	400	50	0.70	925	69.8	2.1	1.1	2.9

r_s	$x_{sd} = x_{rd}$	x_m	r_r	7th harmonic: $x_{m\,7}$
0.0256	0.0679	0.5791	0.0379	0.5791 / 49 = 0.0118

The results are shown in Fig. 8 (solid and broken lines for the voltage and current source, respectively). The instantaneous torque and currents are obtained with the dynamic model in (22)-(24) while the steady-state torque- and current-slip curves are obtained with the steady-state model with truncation from [22] (voltage source) and the model in (28)-(29) (current source). The hypothesis of the stator supplied by a sinusoidal current source is suitable, as the differences between both cases are not significant. As expected from the exaggeration of the harmonic amplitude, the results are rather extreme, especially the large oscillations in the instantaneous torque. Thus, the model seems unable to predict the measured squirrel-cage torque irregularities in Fig. 1, Fig. 2 and Fig. 3.

Two conclusions can be extracted from this analytical model: (1) the harmonic magnitudes must be exaggerated to make their effects on the torque-speed curve visible; (2) it cannot be used directly (without changes) for motors where space harmonic and skin effects are apparent because of the various simplifying assumptions.

10 Acknowledgements

This research work has been supported by the Spanish Ministry of Economy and Competitiveness through project DPI2011-28021.

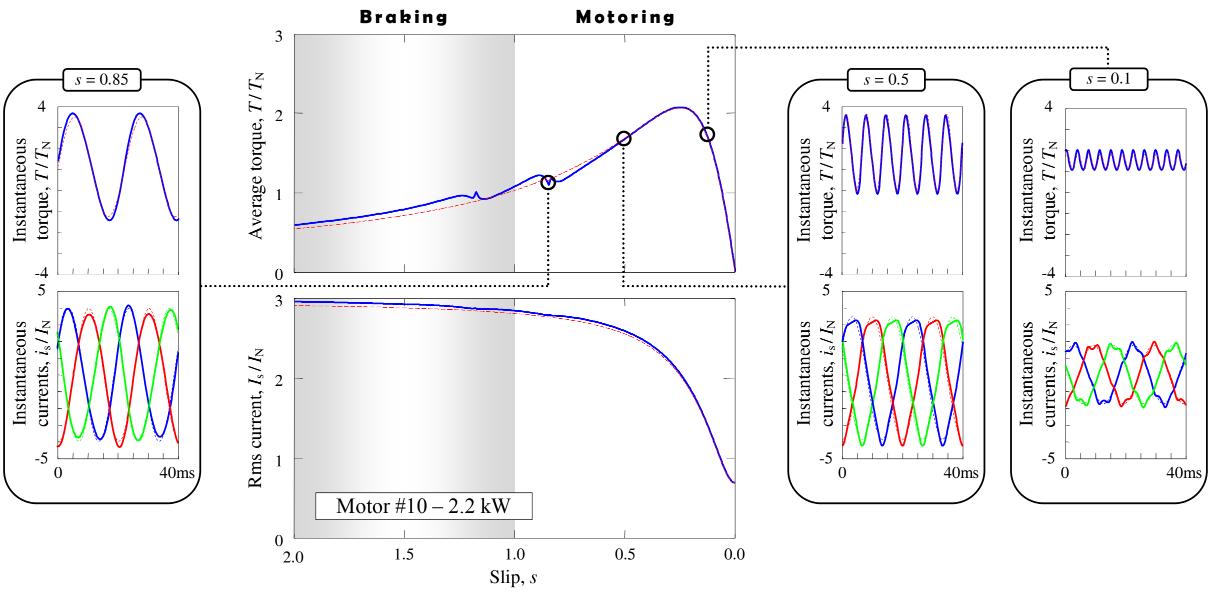

Fig. 8 *Simulated (average) torque and (rms) current-slip curves for the motor of Table 5 assuming non-sinusoidally distributed windings (concentrated windings), uniform air-gap and no skin effect. The instantaneous torque and currents at three different points with slips 0.85, 0.5 and 0.1 are also plotted. The stator is supplied by a sinusoidal voltage source (solid line) and a sinusoidal current source (broken line).*

11 References

1 Boldea, I., Nasar, S. A.: *The Induction Machine Handbook*. 2nd ed. Boca Raton, FL: CRC Press, 2010, pp. 273-286.

2 Hamdi, E. S.: *Design of Small Electrical Machines*. Chichester, England: John Wiley & Sons, 1994, pp. 128-133, 185-228.

3 ABB Oy/Drives, Drive Size v3.8, 2013. Available (3 Apr. 2014): http://www.abb.com

4 European Commission, *EuroDEEM International v. 1.0.17*, 2007. Available (3 Apr. 2014): http://www.sunbird.jrc.it/energyefficiency/eurodeem

5 Agarwal, P. D.: 'Equivalent circuits and performance calculations of canned motors,' *IEEE Trans. on PAS*, *Part III*, 1960, **79** (3), pp. 635-642.

6 Christofides, N.: 'Origins of load losses in induction motors with cast aluminium rotors,' *Proc. of the IEE*, 1965, **112**, (12), pp. 2317-2332.

7 Subba, V., Butler, O. I.: 'Stray losses of polyphase cage-induction motors with particular reference to the condition of imperfect rotor-bar-iron insulation,' *Proc. of the IEE*, 1969, **116**, (5), pp. 737-751.

8 Kron, G.: 'Induction motor slot combinations. Rules to predetermine crawling, vibration, noise and hooks in the speed-torque curve,' *Trans. of the AIEE*, 1931, **50**, (2), pp. 757-767.

9 Robinson, R. B.: 'Inductance coefficients of rotating machines expressed in terms of winding space harmonics,' *Proc. of the IEE*, 1964, **111**, (4), pp. 769-774.

10 Barton, T. H., Dunfield, J. C.: 'Inductances of a practical slip-ring primitive. I - An analytical study,' *IEEE Trans. on PAS*, 1966, **85**, (2), pp. 140-145.

11 Lesenne, J., Notelet, F., Seguier, G.: *Introduction a l'Electrotechnique Approfondie*. Paris: Technique & Documentation, 1981, pp. 33-39.

12 Heller, B., Hamata, V.: *Harmonic field effects in induction machine*. Elsevier, 1977, pp. 115-129.

13 Heartz, R. A., Saunders, R. M.: 'Harmonics due to slots in electric machines,' *IEEE Trans. on PAS, Part III*, 1954, **73**, (2), pp. 946-949.

14 Fudeh, H. R., Ong, C. M. 'Modeling and analysis of induction machines containing space harmonics. Parts I, II and III,' *IEEE Trans. on PAS*, 1983, **102**, (8), pp. 2608-2628.

15 Echevarría-Villar, J.-A., Martinez-Román, J., Serrano-Iribarnegaray, L.: 'Transient harmonic torques in induction machines: measurement and impact on motor performance,' *Electrical Engineering*, 2012, **94**, (2), pp. 67-80.

16 Pedra, J., Córcoles, F., Monjo, Ll., Bogarra, S., Rolán, A.: 'On fixed speed WT generator modeling for rotor speed stability studies,' *IEEE Trans. Power Syst*., 2012, **27**, (1), pp. 397-406.

17 Odok, A. M.: 'Stray-load losses and stray torques in induction machines,' *IEEE Trans. on PAS, Part III*, 1958, **77**, (3), pp. 43-53.

18 Monjo, Ll., Córcoles, F., Pedra, J.: 'Saturation effects on torque- and current-slip curves of squirrel-cage induction motors,' *IEEE Trans. Energy Conv*., 2013, **28**, (2), pp. 243-254.

19 Pedra, J., Córcoles, F.: 'Estimation of induction motor double-cage model parameters from manufacturer data,' *IEEE Trans. Energy Conv*., **19**, (2), pp. 310-317.

20 The MathWorks, Inc., *Matlab 7.9* (*R2009b*). Natick, MA: 2009.

21 Ku, Y. H.: 'Rotating-field theory and general analysis of synchronous and induction machines,' *Proc. IEE - Part IV: Institution Monographs*, 1952, **99**, (4), pp. 410-428.

22 Monjo, Ll, *Aportacions a la modelització de la màquina d'inducció de gàbia d'esquirol*. PhD Dissertation, Jul. 2013 (in Catalan): http://www.tdx.cat/handle/10803/129457, pp. 41-49.